ISSN 0965-5441, Petroleum Chemistry, 2019, Vol. 59, No. 5, pp. 485–497. © Pleiades Publishing, Ltd., 2019.
Russian Text © The Author(s), 2019, published in Nanogeterogennyi Kataliz, 2019, Vol. 4, No. 1, pp. 3–16.

Mechanism of Fischer–Tropsch Synthesis over Nanosized Catalyst Particles: Approaches and Problems of Ab Initio Calculations

A. E. Kuzmin[a, *], M. V. Kulikova[a], and A. L. Maximov[a, b]

[a] *Topchiev Institute of Petrochemical Synthesis, Russian Academy of Sciences, Moscow, 119991 Russia*
[b] *Faculty of Chemistry, Moscow State University, Moscow, 119991 Russia*
**e-mail: kuzmin@ips.ac.ru*

Received December 10, 2018; revised December 25, 2018; accepted January 14, 2019

Abstract—The main results of calculations of energy parameters performed by ab initio methods (DFT) for steps of the mechanism of Fischer–Tropsch synthesis involving cobalt- and iron-containing catalytic systems which have been published over the last decade and a half are analyzed. Primary attention is paid to the results somehow characterizing a transition from catalyst representation as crystallographically ideal surfaces of metals to the realistic models of nanoparticles both homogeneous crystallochemically and containing surface defects and/or heteroatoms. It is shown that little attention is given to the calculations of iron-containing catalysts compared with cobalt-containing ones and the calculations of chain growth steps compared with steps through formation of single-carbon compounds; the methodological problems of applying DFT to nanoparticles suspended in a liquid medium are highlighted.

Keywords: Fischer–Tropsch synthesis, catalytic mechanism, DFT, iron, cobalt
DOI: 10.1134/S0965544119050050

The catalytic synthesis of aliphatic organic compounds, both hydrocarbon (Fischer–Tropsch synthesis, FTS) and oxygen-containing from CO and H_2

$$(2n+1)H_2 + nCO \rightarrow C_nH_{2n+2} + nH_2O, \quad (1a)$$

$$2nH_2 + nCO \rightarrow C_nH_{2n} + nH_2O, \quad (1b)$$

$$2nH_2 + nCO \rightarrow C_nH_{2n+1}OH + (n-1)H_2O, \quad (1c)$$

has been the subject of both academic and applied research for almost a century [1–4]. Nevertheless, in this area, there are still both poorly studied fundamental issues (and mechanistic features are virtually the most important among them) and opportunities for the development of innovative lines of research and their practical implementation.

One of these directions, which has attracted considerable attention in the last decade, is a variant of Fischer–Tropsch synthesis developed by S.N. Khadzhiev et al. [5–7], which stipulates the use of particles of cobalt- or iron-containing nanosized catalysts (~1–100 nm) prepared in situ in a bubbled slurry (high-boiling alkane medium) and performed in it. In this case, it is advisable to consider the active metal of a catalyst in forms almost bordering with homogeneous clusters (with promoting additives or without them) and suspension liquid phase molecules (usually long-chain alkanes) residing in the immediate vicinity of metal particles as a common complex catalytic system for which unusual properties and in principle a peculiar reaction mechanism may be expected. Taking into account that active metal nanosized particles are typical of traditional forms of Fischer–Tropsch catalysts, in which they are deposited on supports ([8–10]) and the reaction is structure-sensitive (review [11]), gaining insight into the detailed mechanism of Fischer–Tropsch synthesis for these particles is a very urgent problem.

The fundamental character of feasible intermediates and elementary reaction steps in this mechanism was ascertained in general by the end of the 20th century [12, 13]; the reaction network of potential routes includes the combinations of steps of classical mechanisms, such as carbide-methylene [14, 15], enol [16, 17], or CO insertion [18, 19], and many steps of hydrogenation/dehydrogenation of intermediates containing several C atoms at different degrees of saturation were added. The network may generally comprise hundreds and even thousands of feasible steps, even if we limit ourselves to C_1 intermediates and products [20]. It is evident, however, that the preponderance of one or another route in a similar network and its limitation by one or another step are determined by differences in the catalyst nature, composition of its modifiers, and structure of its particles which affect the energy/geometry characteristics of surface compounds, heights of activation barriers, and pre-exponential multipliers of elementary reaction steps. Because the experimental values of these characteris-

tics (the more so for the mechanism implemented in situ) are scarce, such a quantitative analysis requires modern ab initio quantum-chemical calculations for heterogeneous catalysis mediated by transition metals, primarily the use of density functional theory (DFT), where description of the system using the N-electron wave function is replaced with description based on the distribution of electron density, in the average field of which electrons move independently of each other [21, 22]. Among various approximations used in DFT calculations for processes occurring on infinite surfaces of crystals, the generalized gradient approximation (GGA) predominates [23]. Within the framework of this approximation (examples will be given in the references below), various versions of Perdew–Wang (PW91) or Perdew–Burke–Ernzerhof (PBE) exchange-correlation functionals for valence electrons and basis sets—plane-waves (PW) or in some cases double zeta plus polarization (DZP) waves in combination with PAW, Troullier–Martins (TMPP), and ultrasoft (USPP) core pseudopotentials—are frequently used. Parameters of the used surface model, such as the mesh size, the number of atomic layers in it (both involved in relaxation during interaction with surface compounds and "frozen"), and the choice of the k-point grid for the Brillouin zone, are of importance. The pathways of elementary reaction steps on PES, particularly, activation barriers, are most frequently determined by the method of nudged elastic band, NEB (C(limbing)I(mage)-NEB is its commonly used modification), although the method of linear/quadratic synchronic transits LST/DST and the method of dimers should be mentioned here.

The quantity of papers published during the last 10–15 years which concern the application of DFT to calculations of the FTS mechanism (as a whole or separate steps assumed by the particular authors to be the most important) is fairly large. In view of the limited volume, the present review, not pretending to present all of the results of these studies, focuses on solving the following tasks:

(1) systematization of the results relevant to difference in the routes of the FTS mechanism over the surfaces of cobalt- or iron-containing systems in order to understand to what extent these results can be applied to the modeling of FTS catalysis by nanoparticles;

(2) special consideration of problems encountered in calculations of activation barriers for C–O bond cleavage and C–C bond formation key steps.

MECHANISM OF FISCHER–TROPSCH SYNTHESIS INVOLVING COBALT-CONTAINING SYSTEMS

The interest in the ab initio calculations of the mechanism of Fischer–Tropsch synthesis mediated by cobalt-containing catalysts is much more pronounced compared with iron-containing systems: it suffices to mention two comprehensive reviews [24, 25] on the matter, whereas iron-containing systems are the subject of only one review and then only partially. However, since its issuance, a number of interesting papers deserving our attention have been published.

Metallic Cobalt Surfaces

As is well known [26, 27], bulk metallic cobalt at temperatures below ≈420–430°C is characterized by the hexagonal close-packed atomic lattice (hcp); at temperatures above ≈420–430°C, by the face-centered cubic lattice (fcc). For nanosized particles, the coexistence of both phases (at different particle sizes) was demonstrated many times by tests both for free metal particles under an inert atmosphere [28] and immediately for Fischer–Tropsch catalysts under synthesis conditions [29, 30] (hcp particles looked more active). Therefore, the attention of researchers was given to surfaces controlled by both lattices, although (as will be seen from the following) interest in hcp surfaces prevails.

The way a particle of a fine metal will appear in terms of predominance of facets with a specific crystallographic index is usually ascertained by the surface matching procedure using the Wulff construction (based on the known Gibbs–Wulff theorem relating the vector normal to the surface to its free energy): the edges and vertices of the particle surface reflect the crystallographic consistency of facets and their relative portion corresponds to the minimum of free energy. For Co particles, an example of applying this procedure [31] is shown in Fig. 1: for an hcp particle, there is a combination of six surfaces with prevailing indices (10-10) and (10-11); for an fcc particle, there are only four surfaces with the dominance of (111). Naturally, the shapes of real nanoparticles in the general case will not follow these equilibrium configurations. However, a set of surfaces proposed in this model may be typical of a fairly wide range of conditions for real synthesis and performance of Fischer–Tropsch catalysts, including metallic Co.

Although for the hcp lattice a considerable region of the surface is occupied by facets with indices (10-10) and (10-11), facet (0001) with the lowest crystallographic index and the closest packing of atoms is the most popular object for calculating the properties of surface compounds—the quantity of studies dealing the mechanism of Fischer–Tropsch synthesis on this facet is almost the same as for all the rest of the surfaces of pure Co taken together. Just various examples of calculating energy characteristics of intermediate compounds and mechanistic steps for Co(0001) can vividly demonstrate the complexity of quantitative agreement of DFT results both with the experimental data and between themselves (the values of activation barriers, Table 1).

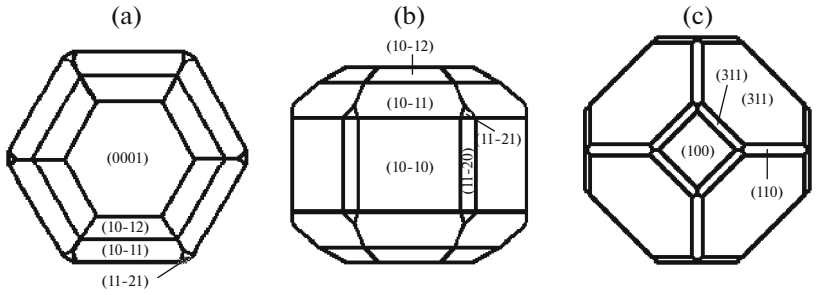

Fig. 1. Models of metallic Co nanoparticles with a set of facets obtained via the Wulff construction ([31]): (a) hcp, view in plane (0001), (b) hcp, view in plane (10-10), and (c) fcc, view in plane (100).

The most evident example is CO adsorption: the experimental value of the binding energy (the highest) for a nondissociated molecule on the above surface is 115 ± 13 kJ/mol [32, 33]; however, all the above-mentioned computational studies yield values overestimated by 0.5–0.7 eV (moreover, they incorrectly predict the preferable coordination of the molecule on three metal atoms, whereas according to LEED spectroscopy [34, 35], the CO on-top coordination is preferred). An estimate close to the experimental value (difference by 5–10 kJ/mol) can be obtained using the RPBE functional instead of PW91 or PBE [36, 37], although not all experimental characteristics of CO adsorbed on cobalt are reproduced by this functional more accurately than PW91 and PBE.

Calculations of the effect of CO surface coverage on the energy parameters of adsorption of Fischer–Tropsch synthesis intermediates were reported in [38–40]. Here it suffices to note that, in the overwhelming majority of cases as CO surface coverage grows, lateral repulsion leads to a decrease in the absorption energy (from small values to ≈100 kJ/mol). The exception is COH, for which at the 0.25 monolayer CO coverage [38] the absorption energy grows by 35 kJ/mol owing to the formation of hydrogen bonds with CO; however, at the 0.5 monolayer CO coverage, it decreases by 63 kJ/mol [39]. It is possible that the reason behind this finding is that not only the surface coverages but also the DFT calculation approaches are different.

The initial steps of the preferential Fischer–Tropsch synthesis route are known to be determined by the character of CO bond cleavage: in the CO direct dissociation—this is the carbide-methylene mechanism—or after formation of hydrogen-containing C_1 intermediates (the onsets of enol route and insertion route). For (0001), the route involving the formation of HCO species (and subsequently CH_2O species) is more preferable [38, 41–43], although the values of calculated activation barriers in these studies may differ considerably. The same is true of the enol route comprising HCO and HCOH species [38, 39]. The highest potential barrier for the cleavage of this bond in HCO is 93 kJ/mol, whereas the calculated values for the direct dissociation barrier are not below 220 kJ/mol (Table 1). However, surface HCO, CH_2O, and HCOH species are unstable and the direct experimental verification of these data remains a very difficult task so far.

The predominance of one or another route may considerably depend on the nature of the concomitant group occupying Co(0001) [36]. If this is the OH group, then the activation barrier for the CO + H coupling to COH (and then to CHOH) is 50 kJ/mol lower compared with CHO formation (in contrast to the case of H coverage); methanol formation is also preferable with respect to any form of C–O bond dissociation (followed by C–C bond formation). In accordance with [36], a small contribution of this route is explained by a small OH surface coverage. The authors of [36] made a general conclusion that Co(0001) is unrepresentative in real catalysis. The preference of the enol route over the CO direct dissociation was predicted in [50]. However, coverage effects were calculated in [50] only for CO (0.25 monolayer); for the CHO formation, the barrier was ≈30 kJ/mol lower than that for the COH formation.

The carbon chain growth via the interaction of monomer intermediates CH_x on (0001) was calculated in [51]. Because of smaller activation barriers, interactions involving methylene intermediate CH_2 were somewhat more preferable than other interactions (Table 2), with one very important exception: the step of alkyl formation $CH_3 + CH_2 \rightarrow CH_3CH_2$. Traditionally, this step is assumed to prevail in the scheme of oxygen-free chain growth. However, there is another way of looking at the situation [52]: the most favorable is CH or CH_2 coupling with CHO followed by C–O bond dissociation just as further chain growth—also via alkyl/alkylene coupling with CHO. The barriers for respective steps are 20–30 kJ/mol lower than the barriers for the direct insertion of CO or the coupling of hydrocarbon intermediates. As was shown by calculations [52], the formation of methanol or aldehydes over metallic Co is hardly probable in accordance with common concepts of Fischer–Tropsch synthesis.

Table 1. Some activation barriers for C–O bond cleavage steps on various metallic Co surfaces calculated using different techniques

Step	Surface	E_a, kJ/mol, DFT functional		
		PW91	PBE	RPBE
CO → C + O	(0001)	367 [39][a], 237 [43][b]	325 [38][c], 220 [42][d]	261 [36]
	(0001)-y	155 [44]		116 [45]
	(10-10)	67 [46]	173 [31], 189 [47][e]	
	(10-11)		117 [31], 144 [47]	
	(11-21)		103 [31]	
	(111)		239 [31], 231 [48][f]	
	(100)		144 [31]	
CO + H → HCO	(0001)	138 [39], 141 [43], 124 [52][g]	121 [38], 145 [42], 126 [49][h]	136 [36]
	(0001)-y		74 [49]	9 [45]
	(10-10)	59 [46]	114 [47]	
	(10-11)		57 [31], 103 [47]	
	(11-21)		99 [31]	
	(111)		130 [48]	
	(100)		97 [31]	
HCO → CH + O	(0001)	89 [39], 39 [43]	87 [38], 90 [42], 70 [49]	93 [36]
	(0001)-y			131 [45]
	(10-10)	50 [46]	51 [47]	
	(10-11)		57 [31], 97 [47]	
	(11-21)		61 [31]	
	(111)		63 [48]	
	(100)		103 [31]	

[a] PW, USPP, (2 × 2) mesh, 4 layers (2 relax.), 18-*k* point Chadi–Cohen grid, CI-NEB.
[b] PW, DSPP, (3 × 3) mesh, 4 layers (2 relax.), Monkhorst–Pack *k*-grid, LST/DST.
[c] PW, PAW, (2 × 2) mesh, 8 layers (4 relax.), CI-NEB.
[d] PW, PAW, (2 × 2) or (3 × 3) mesh, 3 layers (1 relax.), Γ-centered 5 × 5 × 1 or 3 × 3 × 1 *k*-grid, NEB.
[e] PW, PAW, (3 × 2) mesh, 3 layers (2 relax.), CI-NEB.
[f] PW, PAW, mesh, 3 layers (1 relax.), 5 × 5 × 1 Monkhorst–Pack *k*-grid, CI-NEB.
[g] PW, PAW, (3 × 3) mesh, 4 layers (2 relax.), 5 × 5 × 1 Monkhorst–Pack *k*-grid, CI-NEB.
[h] DZP, TMPP, (2 × 2) mesh, 4 layers (2 relax.), 5 × 5 × 1 or 3 × 5 × 1 Monkhorst–Pack *k*-grid.

According to [40, 42], Co insertion on the surface under discussion is sensitive to the extent of CO surface coverage. If these effects are ignored [42], the values of activation barriers turn out to be comparable with those obtained for interactions of hydrocarbon C_1 intermediates. If the effect of co-adsorbed CO is taken into account [40], then CO insertion barriers decrease relative to the above-mentioned ones by 20–25 kJ/mol; for CO dissociation steps, vice versa, they increase. The most favorable chain growth route, as evidenced by calculations [40], is the RC hydrogenation to RCH followed by CO insertion and consecutive hydrogenation to RCH_2CO. The turnover frequency of Fischer–Tropsch synthesis estimated for this route is close to the experimental one.

Also, one should note that, for the above surface, CO insertion via the methyl group bond is characterized by a much higher barrier that that for the rest of the CH_x intermediates (Table 2).

An important issue of FTS selectivity concerns gaining insight into the dependence of the olefin/paraffin ratio on the chain length. For this purpose, for Co (0001), the activation barriers for the hydrogenation of *n*-alkyl groups and alkenes (n = 2–6) were computed both disregarding the van der Waals interactions of adsorbates [55] and taking them into account [56]. For the latter task, a special functional BEEF-wDW was used, which is superior to PBE and RPBE functionals with respect to reproducing the adsorption energy of short-chain hydrocarbons. Alkene → alkyl hydrogenation barriers are within 46–52 kJ/mol, and alkyl → alkane hydrogenation barriers are 62–67 kJ/mol; reduction in the olefin/paraffin ratio with increasing chain length (except the case of

Table 2. Some activation barriers for C–C bond formation steps over Co-containing systems for different surfaces

Step	E_a, kJ/mol, surface				
	(0001)	(0001)-y	(10-11)	(111)	$Co_2C(001)$
$CH_3 + C \rightarrow CH_3C$	91 [51][a]	105 [51]			115 [53]
$CH_3 + CH \rightarrow CH_3CH$	101 [51]	150 [51]	124 [54]	98 [48]	159 [53]
$CH_3 + CH_2 \rightarrow CH_3CH_2$	107 [51], 80 [43]	70 [51]	83 [54]	84 [48]	75 [53]
$CH_2 + C \rightarrow CH_2C$	71 [51]	129 [51]			98 [53]
$CH_2 + CH \rightarrow CH_2CH$	73 [51]	127 [51]	122 [54]	68 [48]	104 [53]
$CH_2 + CH_2 \rightarrow CH_2CH_2$	68 [51], 67 [52]	21 [51]	51 [54]	40 [48]	50 [53]
$CH + C \rightarrow CHC$	88 [51]	189 [51]			
$CH + CH \rightarrow CHCH$	83 [51]	170 [51]	107 [54]	62 [48]	
$CH + CO \rightarrow CHCO$	107 [51], 95 [40][b], 95 [52]	125 [64]	144 [54]	99 [48]	
$CH_2 + CO \rightarrow CH_2CO$	80 [42], 74 [40], 80 [52]		106 [54]	67 [48]	
$CH_3 + CO \rightarrow CH_3CO$	185 [42], 144 [55][c], 140 [52]	141 [55]	148 [54]	133 [48]	

[a] PBE, DZP, TMPP, (2 × 2)–(5 × 2) meshes, 4 layers (2 relax.), Monkhorst–Pack *k*-grids, rough optimization for transition states.
[b] PBE, PW, PAW, (3 × 3) mesh, 3 layers, Γ-centered 3 × 3 × 1 *k*-grid, NEB.
[c] PBE, DZP, TMPP, (3 × 2) mesh, 4 layers (2 relax.), 3 × 4 × 1 Monkhorst–Pack *k*-grid, rough optimization for transition states.

ethylene), in accordance with [56], is consistent and, accordingly, is controlled by just adsorption patterns.

Before we conclude our review of the data on Co(0001), it is important to refer to the results reported in [57]: duplicating the methodological techniques used in [43], the authors of [57] additionally introduced effects of the liquid phase (*n*-hexane, $T = 493$ K, $P = 25$ atm) into the model using the so-called conductor-like screening continuum-based model COSMO. The values of activation barriers for various steps changed insignificantly, and the carbide-methylene mechanism of chain growth remained dominant in both gas- and liquid-phase Fischer–Tropsch synthesis; however, the values of pre-exponential multipliers estimated in terms of the activated complex theory may change quite markedly. For example, the contribution of the CO insertion mechanism increases (although its minor character is preserved) and the rate of CO direct dissociation grows.

Much less data are available for other surfaces of a hcp particle, but they are fairly illustrative. The study [31] in which the hcp and fcc models of particles with ideal facets based on the Wulff construction were obtained has been discussed above; on the basis of calculations, it was inferred that the total activity of hcp particles is higher compared with fcc particles (in agreement with the experiment [29, 30]). The structural sensitivity of facets to the activation barriers of CO direct dissociation or CHO formation is very high [31] (Table 1, Co(0001) > Co(10-10) > Co(10-11) > Co(11-21) for the CO direct dissociation), whereas for the successive CH_x hydrogenation ($x = 0–3$) the sensitivity is low [58]. In accordance with [58], this fact indicates that the total structural sensitivity of the methanation reaction is provided by just the sensitivity of CO dissociation step/steps. In addition to Co(11-20) and Co(10-12), the authors of [59] calculated CO adsorption/dissociation on Co(11-24) (which was absent in the hcp particle model [31]) with the most distinct extended defects (double steps and kinks) among all of the three surfaces and, as in [31], showed that there is tendency toward reduction in the CO dissociation barrier with surface "thinning": Co(11-20) > Co(10-12) > Co(11-24). This observation is consistent with the theoretical analysis done in [46, 60]. In accordance with these studies, reduction in the CO direct dissociation barrier is promoted by the B5-type active sites of defective surfaces (four atoms in the surface layer and one more atom in the layer second from the surface) and even to a higher extent by F6 active sites (four atoms in the surface layer and two atoms in the second layer).

The structural sensitivity of CH_x formation was modeled in [47]. For Co(10-10), CHO formation with the subsequent dissociation to CH or conversion to CH_2O followed by dissociation to CH_2 or hydrogen-assisted dissociation to CH_3 is preferable (methanol formation is atypical); for Co(10-11), the latter two routes involve great difficulties.

To chain growth paths on given surfaces, calculations were extended for Co(10-10) [61] and Co(10-11) [54]. In both cases, CH_2 formation is preferable (and CH formation for Co(10-11) too) and further growth of purely hydrocarbon intermediates is energetically more favorable for CH_2 than the insertion of CO or even CHO (for Co(0001) [52]); in the former case, barriers for respective paths are lower by 50–60 kJ/mol; in the latter case, by 15–20 kJ/mol [54].

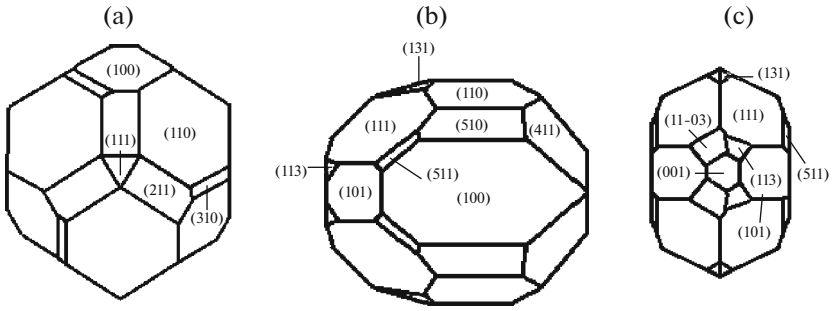

Fig. 2. Models of metallic Fe nanoparticles ([81]) and Hägg carbide Fe_5C_2 ([82]) with a set of surfaces based on the Wulff construction: (a) Fe, view in plane (111); (b) Fe_5C_2, view in plane (100); and (c) Fe_5C_2, view in plane (001).

We note (Table 2) that the chain growth paths involving CH_x species on these surfaces do not necessarily have lower barriers than on (0001).

It is known that extended defects on the crystal surface may be modeled not only by choosing a high Miller index surface (as discussed above) but also by the removal of selected atoms from "low-index" surfaces [44, 45, 49, 51, 62–64]. Reduction in the CO direct dissociation barrier with increasing degree of defectiveness of the surface is also ascertained in this case; formation of a single step on Co(0001) reduces the corresponding activation barrier by 105 kJ/mol ([44], Table 1); formation of a double step, by another 40 kJ/mol [45].

As was shown in [63], for chain growth (CH_y + CH_x and RCH_y + CH_x coupling paths) on Co(0001), the height of barriers for these paths is lower than that on the stepped Co(0001) (except CH_2 + CH_2 and CH_2 + CH_3 paths) [63]. The most favorable routes of C_2 formation on the step are CH_3 + C and CH_2 + CH_2 couplings. For C_3 formation, activation barriers are slightly different from analogous values for C_2 formation (except CH_3C + C and CH_3C + CH couplings, where barriers are lower by 30–35 kJ/mol). For C_4 formation, the difference from C_3 formation is small in any case. In [63], CO insertion routes were not studied at all; in this respect, one must refer to the data from [64], where for the stepped Co(0001) chain growth was predicted to occur predominantly via the insertion route; moreover, these authors pointed out the decisive role of the extent of CO surface coverage for selectivity: if it is small, methane formation is preferred; as the extent of CO surface coverage grows, the probability of chain growth grows as well.

For surfaces of the fcc lattice, C–O bond dissociation also demonstrates structural sensitivity (Table 1 [31, 48]), which manifests itself in a different manner: for example, for the direct dissociation, the transition from (111) to less densely packed surfaces provides reduction in the activation barrier for this pathway; for HCO dissociation, vice versa. The calculations of $\Delta G^{\#}$ performed in [65] for the activation of various steps on Co(111) showed that the CO direct dissociation is also hardly probable; for (100), the direct dissociation is quite feasible. However, according to this model, there is almost no chain growth. This discrepancy with the widespread tendency of cobalt catalysts to produce long-chain hydrocarbons in Fischer–Tropsch synthesis stimulated the authors of [65] to involuntarily change some of the obtained energy parameters (CO direct dissociation barrier, CH_x adsorption energy) to improve consistency of the model results with the experiment. Similar changes were indirectly substantiated by the authors of the cited study by the effects of increased CO surface coverage, because calculations in [65] were done at small surface coverages. Moreover, CO insertion was disregarded in [65]. This also raises additional questions on the completeness of analysis of the data presented in this study and the general character of its predictions. For example, as was shown in [48], for (111), chain growth via the CHO insertion route is more preferable than via the CH_x + CH_y coupling path (as the CO direct insertion). Nevertheless, the formation of methane is more preferable than the formation of higher hydrocarbons [48].

For the fcc lattice, surfaces absent in the particle model (Fig. 2) were also studied. Along with Co(111) and Co(100), surface (211) was taken into account [65]. In contrast to (111), the CO direct dissociation is quite probable on this surface, although the height of the HCO dissociation barrier for this surface is still smaller [66]. The introduction of steps on Co(111) into consideration [65] leads to decrease in methane formation and reduction in barrier for CO hydrogenation to CHO. Finally, Co(321) and Co(221) surfaces characterized by complex extended defects were modeled [67]; the preference of the CO direct dissociation on defective sites (its rate is the highest in the case of kinks) was proved in [67] just as in other situations with fcc and hcp surfaces.

In concluding the discussion of the results available for metallic Co surfaces, it is impossible to disregard the data reported in [68, 69], where the CO conversion to CH was modeled directly in combination with the formation of steps on densely packed surfaces. Steps

are developed (to give rise to nanoislands) as a result of CO dissociation on the above-mentioned B5-type sites followed by the insertion of carbon atoms in the subsurface layer and, what is unusual, by the Co oxidation by this carbon. For this reason the CO absorption energy also increases, and this situation contributes to the further growth of nanoislands. Hydrogenation to CH also occurs mostly on step-edge sites followed by CH migration to terraces, releasing a vacancy for a new CO molecule.

Co Surfaces with Heteroatoms

The paper by Cheng et al. [53] was one of the first studies in which the characteristics of some steps of Fischer–Tropsch synthesis on the surface of Co_2C were calculated. It was predicted that, for the stepped $Co_2C(001)$, CO dissociation activation barriers and methane selectivity grow somewhat relative to the stepped Co(0001). Examination of the other surfaces of this carbide, i.e., (101), (110), and (111) [70], made it possible to show that, for (101) and (110), CH and CH_2 species are dominant (among C_2 intermediates, C_2H_2 and CH_2CH species); for (111), only CH species prevail (among C_2 intermediates, CHCO species). The modeling of surfaces with the metallic Co/Co_2C interface [70, 71] may lead, compared with the initial carbide surface, to the shift of selectivity to the formation of alcohols, thereby making such catalysts similar to systems based on noble metals. However, for (110) and (101), an opposite situation is valid.

Possibly, it would make sense to consider studies dealing with the detailed mechanism of Fischer–Tropsch synthesis on Co surfaces partially covered by atomic carbon in the previous subsection of the present review. Partially covered surfaces Co(0001) and Co(11-21) were examined in [72]; Co(111), in [73]; for the latter surface upon carbonization, the activation barriers for CH_x consecutive hydrogenation steps decreased (about 50–60 kJ/mol), while for chain-growth steps this decrease was somewhat smaller (within 20–50 kJ/mol). According to these data, the authors of [73] made a conclusion that computational results are consistent with the experimentally observed growth of methane formation on the carbonized surface of metallic cobalt.

In accordance with [74], the character of carbon compounds correlates with coefficient α of the molecular-mass distribution of Fischer–Tropsch synthesis products: on the stepped Co(111) with terraces, oligomeric carbon chains prevail (the precursors of graphene or long-chain hydrocarbons) at increased α, while at decreased α, atomic C subsurface insertion and surface reconstruction predominate.

Using Co(11-20) as an example, the authors of [75] explored CO-initiated surface reconstruction for the case of adsorbed K atoms. Because the latter are adsorbed predominantly near the edges of zigzag steps and show the tendency toward surface migration between them, the Co surface is restructured on terraces rather than on steps and this process occurs much more slowly than that in the absence of K. On the whole, these results are in agreement with the physicochemical studies described in [75].

Cobalt promotion by copper was considered in calculations performed in [76, 77]. For Co(0001) [76], the introduction of Cu geometrically controls the ensembles of Co atoms and thus complicates the feasibility of C–O bond cleavage. This facilitates CHO formation, its insertion into the growing chain, and, accordingly, formation of oxygen-containing compounds, in good agreement with general trends of the experimental performance of similar catalysts.

Even through the published data concerning the application of DFT methods to the Fischer–Tropsch synthesis over heteroatomic cobalt systems are scarce, the original paper [78] is worthy of note. The authors of [78] proposed to model a strong metal–support interaction by "inverse catalysts"; that is, systems in which the active metal serves as a support, while the "real" support is introduced as a surface quasi-ligand. Using the example of Co(111) modified with monodentate alumina, it was demonstrated that the CO directly interacts with the quasi-ligand and thus facilitates CO dissociation.

Finally, it is important to pay attention to the data described in [79], where the carbide-methylene mechanism of Fischer–Tropsch synthesis was calculated for small (seven atoms) model clusters representing Co(0001) or Fe(100) modified with Cu, Ag, Au, or Pd atoms and saturated with hydrogen atoms over perimeter to attain a more exact match to the real situation on catalyst surfaces. It is evident that such a representation of the catalytic system makes it possible to use the DFT version without crystal surface approximations (hybrid functional B3PW91, basis set LANL2DZ with implicit core potential, the Berny algorithm for activation barrier determination). However, as follows from the methodical data from the overwhelming majority of the cited papers, this calculation approach was almost never applied to the FTS mechanism. According to [79], Au and Ag are the preferable promoters for Co; for Fe, the preferred promoters are Cu, Ag, and Pd.

MECHANISM OF FISCHER–TROPSCH SYNTHESIS INVOLVING IRON-CONTAINING SYSTEMS

Fischer–Tropsch synthesis over iron-based catalysts attracts much less attention of quantum chemists than cobalt-based counterparts, in contrast to the interest from experimentalists; as was mentioned above, studies addressing the application of DFT methods to iron-containing systems were summarized only in a single review [80].

Table 3. Some values of activation barriers for key steps of C–O bond cleavage over Fe-containing systems calculated for different surfaces using different techniques

Step	Surface	E_a, kJ/mol, DFT functional		
		PW91	PBE	RPBE
$CO \rightarrow C + O$	Fe(100)		101 [84]	105 [83]
	Fe(110)	189 [39]		
	Fe(111)			166 [88][a]; 53–260 [89][b]
	Fe(211)			90 [90]
	Fe_5C_2(001)		287 [91]	83 [92]
	Fe_5C_2(510)		127 [93]	260 [82]
	Fe_5C_2(111)			384 [82]
$CO + H \rightarrow HCO$	Fe(100)		87 [85]	91 [83]
	Fe(110)	89 [39]		
	Fe(111)			124 [88]
	Fe_5C_2(001)		134 [91]	
	Fe_5C_2(510)			86 [82]
	Fe_5C_2(111)			197 [82]
$HCO \rightarrow CH + O$	Fe(100)		73 [85]	62 [83]
	Fe(110)	76 [39]		
	Fe(111)			88 [88]
	Fe_5C_2(001)		112 [91]	196 [92]

[a] PW, PAW, (2 × 2) meshes, 6 layers (3 relax.), 4 × 4 × 1 *k*- Monkhorst–Pack grid, NEB.
[b] PW, PAW, (1 × 1)–(2 × 2) meshes, 7 layers (3 relax.), 5 × 5 × 1 or 3 × 3 × 1 *k*-Monkhorst–Pack grid, NEB.

Metallic Fe at the temperatures of Fischer–Tropsch synthesis and preparation of most catalysts is characterized by the body-centered cubic (bcc) lattice. However, not metallic Fe but Fe_5C_2 carbide (the Hägg carbide) is most often treated as an active crystal phase of FTS. For particles of both crystals, just as for hcp and fcc cobalt lattices, models with sets of facets obtained by the Wulff construction were developed (Fig. 2); therefore, the primary attention in this subsection of the review will be given to just these surfaces.

Metallic Fe Surfaces

In accordance with [81], (100) and (110) are the prevailing surfaces of metallic Fe particles. The CO dissociation on the former surface [83–85] occurs predominantly directly (Table 3) or through HCO formation (depending on CO or H surface coverage, the ratio of these routes may be different), while the formation of COH (and then CHOH) is less favorable. As was shown by calculations [86, 87], chain growth proceeds through C–C bond formation via steps C + CH_2/CH_3/CCH_2/CCH_3, etc., which are followed by H insertion up to the reductive elimination to alkane preferable to β elimination to alkene. CO (HCO) insertion routes were not taken into consideration in the cited papers. For Fe(110) [39] (0.5 monolayer CO coverage), the CO direct dissociation barrier is much higher than that for (100) and even higher than the COH formation barrier (156 kJ/mol). Chain-growth steps were not examined in [39].

When implementing the Wulff construction of a particle, along with its facets, the contributions of atoms located at surface edges or vertices to the mechanism of Fischer–Tropsch synthesis should be taken into account. In the mentioned study [81], this was done for Fe(100-110) edges. The CO dissociation barrier is lower than that for Fe(100) or (110) (in fact, this is similar to the role of extended defects described above for cobalt) and lower than that for edges of Fe icosahedral clusters.

Another surface of metallic Fe which attracts the particular attention from researchers is Fe(111) [88, 89]. CO formation before CO bond cleavage, CH formation, and chain growth via the CH + CH coupling are preferable. The in-depth modeling of the CO direct dissociation on this surface [89] makes it possible to reveal that the barrier for this reaction in the presence of surface C atoms (the autocatalysis of surface carbide formation) decreases substantially, and, as expected, its height strongly depends on adsorption configurations for both the initial CO and the atoms being formed. The boundary values differ very appreciably; therefore, the question arises whether conclu-

Table 4. Some activation barriers for first C–C bond formation steps over Fe-containing systems for different surfaces

Step	E_a, kJ/mol, surface			
	Fe(100)	Fe(111)	Fe_5C_2(001)	Fe_5C_2(510)
$CH_3 + C \rightarrow CH_3C$	83 [86]			119 [95]
$CH_3 + CH \rightarrow CH_3CH$	84 [86]	110 [88]		139 [95]
$CH_3 + CH_2 \rightarrow CH_3CH_2$	144 [86]	102 [88]		144 [95]
$CH_2 + C \rightarrow CH_2C$	82 [86]			104 [95]
$CH_2 + CH \rightarrow CH_2CH$	114 [86]	141 [88]		99 [95]
$CH_2 + CH_2 \rightarrow CH_2CH_2$	146 [86]	102 [88]		100 [95]
$CH + C \rightarrow CHC$	122 [86]			103 [95]
$CH + CH \rightarrow CHCH$	139 [86]	52 [88]		93 [95]
$CH + CO \rightarrow CHCO$		101 [88]	100 [91]	
$CH_2 + CO \rightarrow CH_2CO$		130 [88]		
$CH_3 + CO \rightarrow CH_3CO$		101 [88]		

sions about the role of direct dissociation are unequivocal for other surfaces.

The authors of [90] explored the Fe(211) surface, but only the characteristics of CO adsorption and direct dissociation were calculated. The dissociation barrier was found to be much lower compared with Fe(100) or Fe(111). In accordance with [90], this effect is favored by the slope and stretch of a bond in the three-coordinated CO.

On completion of discussing the studies dealing with Fischer–Tropsch synthesis over metallic Fe, it is important to mention the attempt to model the steps of C–O bond cleavage on an icosahedral nanoparticle encapsulated in the shell composed of carbon atoms, Fe_{55}-C_{240} [94]. These authors were forced to apply the DFT version different from extended-surface models but used some features uncovered in other simulation studies of the mechanism of Fischer–Tropsch synthesis (molecular optimization of double-zeta plus polarization basis set, GTH pseudopotentials). Two-site reaction steps are hardly probable because of the preferable distancing of intermediates from each other. Therefore, it may be stated that the CO insertion mechanism is preferred over carbide and enol ones. However, barriers for C–O bond cleavage steps are much higher than those calculated for ideal surfaces (e.g., for HCO, this value is above 190 kJ/mol; Table 3).

Fe Surfaces Combined with Heteroatoms

As was shown above, the model of the χ-Fe_5C_2 particle with a set of facets based on the Wulff construction was developed in [82]. Modeling studies were limited to CO dissociation steps; in some cases, promoter K_2O was present on the surface being modeled. For (111), (100), (–111), (510), and (–411) surfaces in all cases, the C–O bond dissociation after HCO formation was preferable rather than in the direct way (in any case, at small surface coverage), with direct dissociation barriers being very high (Table 3). However, for facet (510), the total barrier for CH formation through HCO was higher than that through CO direct dissociation (150 versus 127 kJ/mol) because of a high energy level of CH groups [93]. The situation is complicated by the fact that a part of χ-Fe_5C_2 surfaces (such as (001) and (110)) are characterized by the presence of C atoms of the crystal lattice on the surface, and both CO and H and HCO or H_2CO may bind with them and not only with Fe atoms [96].

Among Hägg carbide surfaces, Fischer–Tropsch synthesis was most often modeled for the (001) surface [91, 92, 97]. Among C_1 products, the total energy barrier for methanol is much higher than that for methane [92]; however, HCO preferably converts not to HCOH but to the surface-bound CH_2O and then to CH_3O; the C–O bond in the latter does not cleave before incorporation into the growing chain at least once. Once this cleavage takes place, further chain growth occurs via the carbide mechanism with the systematic involvement of C lattice atoms; the formation of alkanes/alkenes (as exemplified by C_2) is more preferable compared with the corresponding alcohols [91, 97]. It is interesting [91] that water formation through the disproportionation of paired OH groups is preferable rather than the hydrogenation of single OH groups.

For Fe_5C_2(510) a number of activation barriers for chain growth via CH_x coupling paths (Table 4) and for methane formation were calculated [95]; the latter reaction is less favorable than the formation of higher hydrocarbon products. CO insertion was not considered in this paper.

In addition, the attention of researchers was focused on the pattern of Fischer–Tropsch synthesis on the surfaces of other iron carbides, such as $Fe_3C(100)$ [98] (dissociation of the C–O bond after formation of the surface formyl and formation of C_2H_x intermediates by C_sCO hydrogenation involving the lattice carbon atom) or $Fe_3C(031)$ [99] (chain growth via coupling of methylene or methylidene groups is preferable to methane formation). Certain attention was also given to $Fe_2C(001)$ [100] (although CO dissociation and the subsequent chain growth step are hindered here, at increased surface coverage, the formation of bridge CO adsorption on one Fe atom and one C atom was unraveled) and Fe_4C (100), (110), (111) [101] (in all cases the formation of predissociation intermediate—ketene C=C=O—is possible).

A very important aspect of catalysis of Fischer–Tropsch synthesis over iron carbides—the presence of point defects (vacancies) on their surfaces—was investigated [102]. For $Fe_2C(011)$, $Fe_5C_2(010)$, $Fe_3C(001)$, and $Fe_4C(100)$, the unhindered hydrogenation of surface C atoms of the lattice and a marked decrease in the energy barrier for the dissociation of CO adsorbed next to the formed vacancy were predicted; on $Fe_2C(011)$ and $Fe_5C_2(010)$, CH_4 was predominantly formed. Generally, similar conclusions were made for $Fe_5C_2(001)$ [91, 92]. However, for $Fe_5C_2(010)$, reduction in the height of activation barriers is small (≈10 kJ/mol) compared with nonvacant sites in the case of both CO direct dissociation and C–O bond cleavage after HCO formation [103].

In addition, calculations of the adsorption of higher *n*-alkanes and α-alkenes on the surfaces of various carbides allowing for van der Waals interactions (the use of the special functional vdW-DF2) should be mentioned [104]. For χ-$Fe_5C_2(010)$, $Fe_7C_3(001)$, θ-$Fe_3C(001)$, and η-$Fe_2C(011)$, the adsorption energy was independent of chain length beginning from three (alkyls), four (alkanes), and five (alkenes) C atoms. Sorption is the most favorable: for alkanes, on smooth θ-$Fe_3C(001)$; for alkenes, on χ-$Fe_5C_2(010)$; and for alkyls, on any carbon-rich surface.

Furthermore, the data reported in [105] deserve attention, although they do not concern calculations of Fischer–Tropsch synthesis mechanism. However, it can be said that, for the diverse forms of carbide clusters Fe_xC_y ($x, y \le 8$) (here it is also interesting to mention the calculation technique—the Monte Carlo method combined with the DNP basis set, PBE, and DSPP pseudopotential for DFT), C atoms predominantly concentrate on their surface individually or as dimer structures (the latter is not realized for the crystal lattices of iron carbides).

Along with [82], the effect of K (or Na) promotion was modeled in [106] for $Fe_5C_2(100)$ (CO adsorption becomes stronger) and in [107] for Fe(100). It was found that in both cases the absorption energy grows; this effect was primarily attributed to electrostatic effects.

Copper promotion of Fe(100) (atomic co-adsorption, substitution of Fe atoms, formation of the atomic film) and its effect on CO adsorption and dissociation were studied in [108, 109]. The direct dissociation barrier in the presence of the promotor rises appreciably, and the absorption energy in the case of substitution of Fe atoms decreases much more strongly than that in the other two cases.

Finally, interesting results were obtained for Fe(100) modification with palladium [110]. Compared with Cu promotion of the same surface, the CO dissociation is hindered (especially with increased Pd content), and its specific route predominantly involves HCO rather than CHO or the direct dissociation of adsorbed CO.

Even though a large body of published data relevant to DFT calculations of the Fischer–Tropsch synthesis mechanism has been accumulated up to now, it includes substantial gaps demanding filling. As was shown above, the iron-containing catalysts received less attention than the cobalt-containing ones; steps of the mechanism describing the C–C bond formation aroused less attention than CO dissociation and formation of C_1 products. Surprisingly, there is no interest of researchers in calculations of the mechanism of Fischer–Tropsch synthesis involving oxides—both of cobalt and iron—although in real catalysis there is no complete reduction of the metallic component, and the modeling of surfaces with the interfacial boundary, for example, Co/CoO, may yield interesting results valuable in practice. Gaps in DFT calculations in relation to the equivalent representation of processes occurring on all facets appearing in the Wulff construction of the surface of particles of a particular active phase and the consideration of point surface defects for Co and extended defects for Fe or Fe carbides are also evident. It is important to note the problem common for all ab initio calculations of any complex tasks—disagreement of the results obtained for identical systems using different DFT versions; the characteristic example in the covered area is barriers for the CO direct dissociation on Co(0001).

The second important (and challenging for further development of theoretical and computational studies in this particular direction) conclusion of this review is that, for adequate modeling of catalytic systems developed by the Khadzhiev team, the existing methodological DFT basis may be insufficient. The description of interaction of long-chain alkanes of the liquid medium with surface atoms of catalyst particles and with compounds involved in Fischer–Tropsch synthesis, including the resulting long-chain alkanes/alkenes, requires explicitly taking into account van der Waals interactions for them (as was done through the introduction of the BEEF-vDW [56] or vdW-DF2 functionals [104]) and liquid-phase effects (COSMO

[57] or COSMO-RS model; note that, because in the mentioned study *n*-hexane was taken as a liquid phase, the need to consider much heavier alkanes may add computational difficulties). Moreover, particles of the active catalytic phase (regardless of their composition) may be so small that in this case we should focus on the icosahedral packing of atoms; accordingly, both Wulff surface constructions and DFT calculation techniques based on basis sets and functionals optimal for supermeshes of crystal surfaces become unacceptable. In the reviewed papers, Fischer–Tropsch synthesis on the icosahedral particle was explored only in [90] (although it is worth recalling that a particle consisting of 55 Fe atoms is even much smaller than those which were obtained experimentally [5–7]) using a peculiar set of DFT tools different from the above-mentioned approaches for catalysis on infinite surfaces and model clusters composed of a few atoms similar to those examined in [79, 105]. Evidently, the correct combination of all the mentioned techniques in the model scheme (if it is possible at all) free of internal contradictions and its experimental verification are a nontrivial task.

ACKNOWLEDGMENTS

This work performed at the Topchiev Institute of Petrochemical Synthesis, Russian Academy of Sciences, was supported by the Russian Science Foundation (project no. 17-73-30046).

REFERENCES

1. I. B. Rapoport, *Synthetic Liquid Fuel*. Part 2. *Synthesis of Motor Fuels from Carbon Monoxide and Hydrogen* (Gostoptekhizdat, Moscow, 1950) [in Russian].
2. H. H. Storch, N. Golumbic, and R. B. Anderson, *The Fischer-Tropsch and Related Synthesis* (Wiley, New York, 1951; Inostrannaya Literatura, Moscow, 1954).
3. G. Henrici-Olivé and S. Olivé, *The Chemistry of the Catalyzed Hydrogenation of Carbon Monoxide* (Springer, Berlin, 1984).
4. R. B. Anderson, *The Fischer-Tropsch Synthesis* (Academic, New York, 1984).
5. S. N. Khadzhiev, A. S. Lyadov, M. V. Krylova, and A. Yu. Krylova, Pet. Chem. **51**, 24 (2011).
6. M. V. Kulikova and S. N. Khadzhiev, Pet. Chem. **57**, 1173 (2017).
7. M. V. Kulikova, O. S. Dement'eva, A. E. Kuz'min, and M. V. Chudakova, Pet. Chem. **56** (12), 1140 (2016).
8. C. S. Kellner and A. T. Bell, J. Catal. **75**, 251 (1982).
9. G. L. Bezemer, J. H. Bitter, H. P. C. E. Kuipers, and H. Oosterbeek, J. E. E. Holewijn, X. Xu, F. Kapteijn, A. J. van Dillen, and K. P. De Jong, J. Am. Chem. Soc. **128**, 3956 (2006).
10. V. R. R. Pendyala, G. Jacobs, W. Ma, J. L. S. Klettinger, C. H. Yen, and B. H. Davis, Chem. Eng. J. **249**, 279 (2014).
11. Q. Zhang, W. Deng, and Y. Wang, J. Energy Chem. **22**, 27 (2013).
12. C. K. Poorter, Chem. Rev. **81**, 447 (1981).
13. M. E. Dry, Appl. Catal., A **138**, 319 (1996).
14. F. Fischer and H. Tropsch, Brennstoff-Chem. **7**, 97 (1926).
15. V. A. A. van Barneveld and V. Ponec, J. Catal. **88**, 382 (1984).
16. J. T. Kummer and P. H. Emmett, J. Am. Chem. Soc. **75**, 5177 (1953).
17. Ya. T. Eidus, Russ. Chem. Rev. **36**, 338 (1967).
18. H. Pichler and H. Schulz, Chem. Ing. Tech. **42**, 7162 (1970).
19. G. Henrici-Olive and S. Olive, Angew. Chem., Int. Ed. Engl. **55,** 136 (1976).
20. O. N. Temkin, A. V. Zeigarnik, A. E. Kuz'min, L. G. Bruk, and E. V. Slivinskii, Russ. Chem. Bull. **51**, 1 (2002).
21. W. Koch and M. C. Holthausen, *A Chemist's Guide to Density Functional Theory* (Wiley-VCH, Weinheim, 2002), 293 p.
22. C. J. Cramer and D. G. Truhlar, Chem. Phys. Phys. Chem. **11**, 10757 (2009).
23. A. E. Matsson, P. A. Schultz, M. P. Desjarlais, T. R. Matsson, and K. Leung, Model. Numer. Simul. Mater. Sci. **13,** 1 (2005).
24. Y. Qi, J. Yang, D. Chen, and A. Holmen, Catal. Lett. **145**, 145 (2015).
25. X. Xu, P. Tian, Y. Cao, J. Xu, and Y. Han, Chem. Model. **12**, 184 (2016).
26. S. R. Houska, B. L. Averbach, and M. Cohen, Acta Metall. **8**, 81 (1960).
27. B. W. Lee, R. Alsenz, A. Ignatiev, and M. A. van Hove, Phys. Rev. **17**, 1510.
28. O. Kitakami, H. Sato, Y. Shimada, F. Sato, M. Tanaka, Phys. Rev. **56**, 13849.
29. M. K. Gnanamani, G. Jacobs, W. D. Shafer, and B. H. Davis, Catal. Today **215**, 13 (2013).
30. H. Karaca, O. V. Safonova, S. Chambrey, P. Fongarland, P. Roussel, A. Griboval-Constant, M. Lacroix, and A. Y. Khodakov, J. Catal. **277**, 14 (2011).
31. J.-X. Liu, H. Y. Su, D.-P. Sun, B.-Y. Zhang, and W.-X. Li, J. Am. Chem. Soc. **135**, 16284 (2013).
32. S. E. Mason, I. Grinberg, and A. M. Rappe, Phys. Rev. **69**, 161401.
33. F. Ablid-Pedersen and M. P. Andersson, Surf. Sci. **601**, 1747 (2007).
34. M. E. Bridge, C. M. Comrie, and R. M. Lambert, Surf. Sci. **67**, 393 (1977).
35. H. Papp, Surf. Sci. **601**, 5571 (1983).
36. S. Liu, Y.-W. Li, J. Wang, and H. Jiao, Catal. Sci. Technol. **6**, 8336 (2016).
37. B.-T. Teng, X.-D. Wen, M. Fan, F.-M. Wu, and Y. Zhang, Phys. Chem. Chem. Phys. **16**, 18563 (2014).
38. Y. Qi, J. Yang, X. Duan, Y.-A. Zhu, D. Chen, and A. Holmen, Catal. Sci. Technol. **4**, 3534 (2014).
39. M. Ojeda, R. Nabar, A. U. Nilekar, A. Ishikawa, M. Mavrikikakis, and E. Iglesia, J. Catal. **272**, 287 (2010).
40. M. K. Zhuo, A. Borgna, and M. Saeys, J. Catal. **297**, 217 (2013).

41. J. R. Inderwildi, S. J. Jenkins, and D. A. King, J. Phys. Chem. **112**, 1305.
42. M. K. Zhuo, K. F. Tan, A. Borgna, and M. Saeys, J. Phys. Chem. **113**, 8357.
43. A. Asiaee and K. M. Benjamin, Mol. Catal. **436**, 218 (2017).
44. X. Q. Gong, R. Raval, and P. Hu, Surf. Sci. **562**, 247 (2004).
45. C. F. Huo, Y.-W. Li, J. G. Wang, and H. J. Jiao, J. Phys. Chem. **112**, 14108.
46. S. Shetty and R. A. van Santen, Phys. Chem. Chem. Phys. **12**, 6330 (2010).
47. R. Zhang, F. Liu, Q. Wang, B. Wang, and D. Li, Appl. Catal., A **525**, 76 (2016).
48. C. Chen, Q. Wang, G. Wang, B. Hou, L. Jia, and D. Li, J. Phys. Chem. **120**, 9132.
49. J. Cheng, P. Hu, P. Ellis, S. French, G. Kelly, and S. M. Lok, J. Phys. Chem. **112**, 9464.
50. Y. Qi, J. Yang, X. Duan, Y.-A. Zhu, D. Chen, and A. Holmen, Catal. Sci. Technol. **4**, 3534 (2014).
51. J. Cheng, X. Q. Gong, P. Hu, S. M. Lok, P. Ellis, and S. French, J. Catal. **254**, 285 (2008).
52. G. Wen, Q. Wang, R. Zhang, D. Li, and B. Wang, Phys. Chem. Chem. Phys. **18**, 27272 (2016).
53. J. Cheng, P. Hu, P. Ellis, S. French, G. Kelly, and S. M. Lok, J. Phys. Chem. **114**, 1085.
54. H. Liu, R. Zhang, L. Ling, Q. Wang, B. Wang, and D. Li, Catal. Sci. Technol. **7**, 3758 (2017).
55. J. Cheng, T. Song, P. Hu, S. M. Lok, P. Ellis, and S. French, J. Catal. **255**, 20 (2008).
56. Y. Qi, C. Ledesma, J. Yang, X. Duan, Y.-A. Zhu, A. Holmen, and D. Chen, J. Catal. **349**, 110 (2017).
57. A. Asiaee and K. M. Benjamin, Mol. Catal. **436**, 210 (2017).
58. J. -X. Liu, H. Y. Su, and W.-X. Li, Catal. Today **215**, 36 (2013).
59. Q. F. Ge and M. Neurock, J. Phys. Chem. B **110**, 15368 (2006).
60. R. A. van Santen, I. M. Ciobica, E. van Steen, and M. M. Ghouri, Adv. Catal. **54**, 121 (2011).
61. R. Zhang, L. Kang, H. Liu, L. He, B. Wang, Comput. Mater. Sci. **145**, 263 (2018).
62. X. Q. Gong, R. Raval, and P. Hu, J. Chem. Phys. **122**, 024711 (2005).
63. J. Cheng, P. Hu, P. Ellis, S. French, G. Kelly, and S. M. Lok, J. Catal. **257**, 221 (2008).
64. H.-Y. Su, Y. Zhao, J.-X. Liu, K. Sun, and W.-X. Li, Catal. Sci. Technol. **7**, 2967 (2017).
65. P. van Helden, J.-A. van den Berg, M. A. Petersen, W. Janse van Rensburg, I. M. Ciobica, and J. van de Loosdrecht, Faraday Discuss. **197**, 117 (2017).
66. P. van Helden, J.-A. van den Berg, and I. M. Ciobica, Catal. Sci. Technol. **2**, 491 (2012).
67. M. A. Petersen and J.-A. van den Berg, I. M., Ciobica, and P. van Helden, ACS Catal. **7**, 1984 (2017).
68. A. Banerjee, A. P. van Bavel, H. P. C. E. Kuipers, and M. Saeys, ACS Catal. **7**, 5289 (2017).
69. A. Banerjee, A. P. van Bavel, H. P. C. E. Kuipers, and M. Saeys, ACS Catal. **5**, 4756 (2015).
70. R. Zhang, G. Wen, H. Adidharma, A. G. Russell, B. Wang, M. Radosz, and M. Fan, ACS Catal. **7**, 8285 (2017).
71. Y.-P. Pei, J.-X. Liu, Y.-H. Zhao, Y.-J. Ding, T. Liu, W.-D. Dong, H.-J. Zhu, H.-Y. Su, L. Yan, J.-L. Li, and W.-X. Li, ACS Catal. **5**, 3620 (2015).
72. L. Joos, I. A. W. Filot, S. Cottenier, E. J. M. Hensen, M. Waroquier, V. van Speybroeck, and R. A. van Santen, J. Phys. Chem. **118**, 5317.
73. P. Zhai, P-P. Chen, J. Xie, J. -X. Liu, H. Zhao, L. Lin, B. Zhao, H.-Y. Su, Q. Zhu, W.-X. Li, and D. Ma, Faraday Discuss. **197**, 207 (2017).
74. M. Valero Corral and P. Raybaud, J. Phys. Chem. **118**, 22479.
75. M. D. Stroemsheim, I.-H. Svenum, M. H. Farstad, Z. Li, L. Gavrilovic, X. Guo, S. Lervold, A. Borg, and H. J. Venvik, Catal. Today **299**, 37 (2018).
76. X.-C. Xu, J. Su, P. Tian, D. Fu, W. Dai, W. Mao, W.-K. Yuan, J. Xu, and Y.-F. Han, J. Phys. Chem. **119**, 216 (2015).
77. G. Prieto, S. Beijer, M. L. Smith, M. He, Y. Au, Z. Wang, D. A. Bruce, K. P. de Jong, J. J. Spivey, and P. E. de Jongh, Angew. Chem., Int. Ed. Engl. **53**, 6397 (2014).
78. T. van Heerden and E. van Steen, Faraday Discuss. **197**, 87 (2017).
79. P. C. Psarras and D. W. Ball, Comput. Theor. Chem. **1063**, 1 (2015).
80. J. L. C. Fajin, M. N. D. S. Cordeiro, and J. R. B. Gomes, Catalysts **5**, 3 (2015).
81. M. Melander and K. Laasonen, J. Mol. Catal. A: Chem. **406**, 31 (2015).
82. S. Zhao, X.-W. Liu, C.-F. Huo, X.-D. Wen, W. CaoD, Guo, Y. Yang, Y.-W. Li, J. Wang, and H. Jiao, Catal. Today **261**, 93 (2016).
83. M. R. Elahifard, M. P. Jigato, and J. W. Niemantsverdriet, Chem. Phys. Chem. **13**, 89 (2012).
84. S. Amaya-Roncancio, D. H. Linares, K. Sapag, and M. I. Rojas, Appl. Surf. Sci. **346**, 438 (2015).
85. S. Amaya-Roncancio, D. H. Linares, H. A. Duarte, and K. Sapag, J. Phys. Chem. **120**, 10830.
86. J. M. H. Lo and T. Ziegler, J. Phys. Chem. **111**, 13149.
87. J. M. H. Lo and T. Ziegler, J. Phys. Chem. **112**, 13681.
88. H.-J. Li, C.-C. Chang, and J.-J. Ho, J. Phys. Chem. **115**, 11045.
89. S. Booyens, M. Bowker, and D. J. Willock, Surf. Sci. **625**, 69 (2014).
90. D. Borthwick, V. Fiorin, S. J. Jenkins, and D. A. King, Surf. Sci. **602**, 2325 (2008).
91. D.-B. Cao, Y.-W. Li, J. Wang, and H. Jiao, J. Mol. Catal. A: Chem. **346**, 55 (2011).
92. M. O. Ozbek and J. W. Niemantsverdriet, J. Catal. **325**, 9 (2015).
93. T. H. Pham, X. Duan, G. Qian, X. Zhou, and D. Chen, J. Phys. Chem. **118,** 10170.
94. G. Cilpa-Karhu and K. Laasonen, Phys. Chem. Chem. Phys. **20**, 2741 (2017).
95. T. H. Pham, Y. Qi, J. Yang, X. Duan, G. Qian, X. Zhou, D. Chen, and W. Yuan, ACS Catal. **5**, 2203 (2015).

96. D.-B. Cao, F-Q. Zhang, Y.-W. Li, J. Wang, H. Jiao, J. Phys. Chem. B **109**, 10922.

97. D.-B. Cao, S.-G. Wang, Y.-W. Li, J. Wang, H. Jiao, J. Mol. Catal. A: Chem. **272**, 275 (2007).

98. L.-J. Deng, C.-F. Huo, X.-W. Liu, X.-H. Zhao, Y.-W. Li, J. Wang, and H. Jiao, J. Phys. Chem. **114**, 21585.

99. Y. Wang, Y. Li, S. Huang, J. Wang, H. Wang, J. Lv, and X. Ma, Chem. Phys. Lett. **682**, 115 (2017).

100. X. Yu, X. Zhang, Y. Meng, Y. Zhao, Y. Li, W. Xu, Z. Liu, Appl. Surf. Sci. **434**, 464 (2018).

101. C.-M. Deng, C.-F. Huo, L.-L. Bao, G. Feng, Y.-W. Li, J. Wang, and H. Jiao, J. Phys. Chem. **112**, 19018.

102. C.-F. Huo, Y.-W. Li, J. Wang, and H. Jiao, J. Am. Chem. Soc. **131**, 14713 (2009).

103. M. A. Petersen and W. J. van Rensburg, Top. Catal. **58**, 665 (2015).

104. J. G. de la Cruz, M. K. Sabbe, and M.-F. Reyniers, J. Phys. Chem. **121**, 25052.

105. L. Zheng, X. Liu, Y. Meng, Y. Zhou, Y. Yang, H. Jiao, Y.-W. Li, X.-D. Wen, W. Guo, and Q. Peng, Phys. Chem. Chem. Phys. **18**, 32944 (2016).

106. M. A. Petersen, M. J. Cariem, M. Claeys, and E. van Steen, Appl. Catal., A **496**, 64 (2015).

107. M. H. Mahyuddin, R. V. Belosludov, M. Khazaei, H. Mizuseki, and Y. Kawazoe, J. Phys. Chem. **115**, 23893.

108. M. R. Elahifard, E. Fazeli, A. Joshani, and M. R. Gholami, Surf. Interface Anal. **45**, 1081 (2013).

109. X. Tian, T. Wang, Y. Yang, Y.-W. Li, J. Wang, and H. Jiao, J. Phys. Chem. **118**, 20472.

110. W. Wang, Y. Wang, and G.-C. Wang, J. Phys. Chem. **121**, 6820.

Translated by T. Soboleva